SCIENCE CHINA
Technological Sciences

•Article•

February 2023 Vol.66 No.2: 560–573
https://doi.org/10.1007/s11431-022-2284-9

Design and numerical analysis of serpentine microchannel integrated with inner-wall ridges for enhanced droplet mixing

CAO Xiang[1] & CHEN YongPing[1,2*]

[1] *Key Laboratory of Energy Thermal Conversion and Control of Ministry of Education, School of Energy and Environment, Southeast University, Nanjing 210096, China;*
[2] *Jiangsu Key Laboratory of Micro and Nano Heat Fluid Flow Technology and Energy Application, School of Environmental Science and Engineering, Suzhou University of Science and Technology, Suzhou 215009, China*

Received September 6, 2022; accepted December 12, 2022; published online January 30, 2023

A numerical model is developed for three-dimensional droplet mixing in serpentine microchannels with inner-wall ridges (referred to as SMR microchannels). The underlying mechanisms of mixing in SMR microchannels are revealed, and the effects of the ridge width and ridge number on mixing inside droplets of different sizes are clarified. The results indicate that SMR microchannels are capable of enhancing the mixing efficiency by 3.6%–12.5% compared with that in smooth serpentine microchannels, particularly when the droplet length is larger than the microchannel width and the width ratio of the ridge to the microchannel is 0.25–1. The above mixing enhancement is determined by two main factors: the combined effects of the vortex pair and reverse flow, and non-horizontal vortices. Moreover, when the width ratio is 1, there is a maximum 16.0% increase in mixing efficiency for small droplets with a length equal to the microchannel width. However, for small droplets, mixing in an SMR microchannel is worse than in a smooth serpentine microchannel when the width ratio is less than 0.75. With increasing the ridge number, when the width ratio is 0.25, the mixing efficiency is reduced for small droplets but increased for larger droplets.

droplet, mixing, serpentine microchannel, ridge, microfluidics

Citation: Cao X, Chen Y P. Design and numerical analysis of serpentine microchannel integrated with inner-wall ridges for enhanced droplet mixing. Sci China Tech Sci, 2023, 66: 560–573, https://doi.org/10.1007/s11431-022-2284-9

1 Introduction

Owing to the high-throughput [1], high-efficiency [2], and low-cost characteristics [3] of droplet-based microfluidics in microchemical processes [4,5] and bioengineering [2,6], droplet mixing as a basic operation has attracted increasing attentions. However, in the Stokes flow regime of most microfluidics, mixing is dominated by molecular diffusion, which is inefficient [7,8] and unable to satisfy high-throughput droplet-based tests [9]. Therefore, to enhance the performance of droplet mixing in microchannels, chaotic advection has been introduced, which does not require the much larger pump necessary for high-efficiency turbulent mixing [10,11]. Because of the stretching and folding of chaotic flows, the diffusive distance between each component can be significantly reduced, thereby achieving efficient chaotic mixing [8,10]. In addition, the chaotic mixing processes inside droplets have been demonstrated to be sensitive to multiple factors, such as microchannel geometrical characteristics [5,6,12–14], fluid physical properties [15], droplet size [13], and flow conditions [16]. It should be noted that chaotic advection cannot always guarantee effective mixing, due to the possible coexistence of poorly mixed islands with finely mixed regions [17,18]. Therefore, there is growing interest in designing a microchannel structure that enables highly efficient chaotic mixing inside droplets. To overcome

*Corresponding author (email: ypchen@seu.edu.cn)

the limitations of traditional straight and symmetric microchannels in inducing chaotic mixing inside droplets [7], several simple serpentine microchannels were introduced by Song et al. [9,12]. Numerical modeling and visual investigations were subsequently performed for the serpentine microchannels [14,19]. Serpentine microchannels are popular and effective due to their simple structure and good chaotic mixing performance, thus, numerous theoretical and experimental studies have been devoted to droplet mixing in these channels.

Accordingly, the development of channel structures based on serpentine microchannels has drawn increasing attention in droplet mixing. Several serpentine microchannels with structural modifications have recently been proposed, that achieved considerable improvements in chaotic mixing inside droplets and triggered an increase in research on modified serpentine microchannels with high mixing performance. For example, a serpentine microchannel with asymmetric arched bumps on the side walls, called a bumpy serpentine microchannel, was proposed by Liau et al. [6] to improve droplet mixing, and experiments demonstrated that effective droplet mixing was achieved in milliseconds. Liau et al. [6] explained that improvement in mixing was caused by the enhanced fluid circulation within the droplets and the increased asymmetry of the circulation, which were induced by the bumps arranged on one side of the microchannel. A parametric investigation was then conducted by Yin and Luo [15] to reveal the mixing mechanism of the bumpy serpentine microchannel through numerical modeling based on the coupling level-set method and immersed-boundary method. The results indicated that the asymmetry of the vortex pair within droplets was enlarged by increasing the viscosity ratio or bump curvature, giving rise to enhanced droplet mixing. However, the study by Yin and Luo [15] focused on the hydrodynamic characteristics inside droplets flowing through a single bumpy section with no consideration of the three-dimensional (3D) mixing characteristics in the entire microchannel. Cao et al. [20] numerically simulated 3D droplet mixing in a bumpy serpentine microchannel with rectangular bumps on the side walls. They found that droplet mixing in a serpentine microchannel with outside bumps was better than that with inside bumps, and observed optimal mixing performance in a serpentine microchannel with outside bumps when the interval between adjacent bumps was comparable to the droplet length. According to the above discussion, structural modifications can increase the asymmetry of vortexes inside droplets by introducing constricted structures in serpentine microchannels, thereby enhancing droplet mixing. However, constriction of microchannels is considered to result in a significant increase in pressure loss [20,21] and a higher breakage probability of large droplets [22]. Instead, constricting microchannels, Stroock et al. [23] presented a 3D twisting flow that was generated in a straight micromixer broadened by oblique ridges on the walls, which induced efficient chaotic mixing in single-phase flow. Although a ridge structure has been presented to improve single-phase mixing, droplet mixing can be enhanced by increasing the asymmetry of the vortex inside droplets with the help of a 3D twisting flow. Moreover, a broadened microchannel can help control the pressure loss and reduce the breakage probability of large droplets.

In summary, it is meaningfully required to investigate 3D droplet mixing characteristics and hydrodynamics in a serpentine microchannel with the new structural design consisting of ridges, namely, SMR microchannel. The effects of the ridge structure on the droplet mixing performance are important for understanding the mixing mechanism and improving the design of SMR-microchannel mixers. Therefore, to investigate droplet mixing in SMR microchannels, a coupled model of the volume-of-fluid (VOF) method and component transfer equation was developed. Then, a numerical study was conducted to reveal the underlying mechanisms of the mixing in an SMR microchannel in comparison with that in a traditional smooth serpentine microchannel. In addition, the effects of two important geometric parameters of ridges, (i.e., ridge width and ridge number) on the mixing performance of droplets with different sizes were investigated and clarified.

2 Mathematical model

2.1 Geometry of a serpentine microchannel with inner-wall ridges (SMR microchannel)

In order to study the droplet mixing performance and hydrodynamic characteristics of droplets, an SMR microchannel was constructed with inner-wall ridges as depicted in Figure 1. The SMR microchannel consists of a straight inlet channel with a length L of 450 μm for ordering the droplet, a straight outlet channel with a length L_2 of 200 μm, and a serpentine channel with a span L_s of 280 μm and radius R of 120 μm. The cross section of the SMR microchannel square with width w was 80 μm, and ridges with height $h_r = 0.5w$ were obliquely arranged on the walls at an angle $\theta = 63°$ with respect to the tangent of the curved channel to induce a 3D twisting flow in the channel [23,24]. To comprehensively understand the droplet mixing mechanism, two geometric parameters of the ridge, namely, the ridge width (w_r) and ridge number (n), were investigated under various droplet sizes. The droplet size was evaluated by the dimensionless droplet length $l_d^* = l_d/w$, where l_d represents the droplet length along the flow direction in the straight inlet channel (see Figure 1(a)). A home-made program was introduced to generate equally sized droplets, and controlled the droplet volume by limiting the duration of injection. The ridge width is represented by the non-dimensional parameter $w_r^* = w_r/w$.

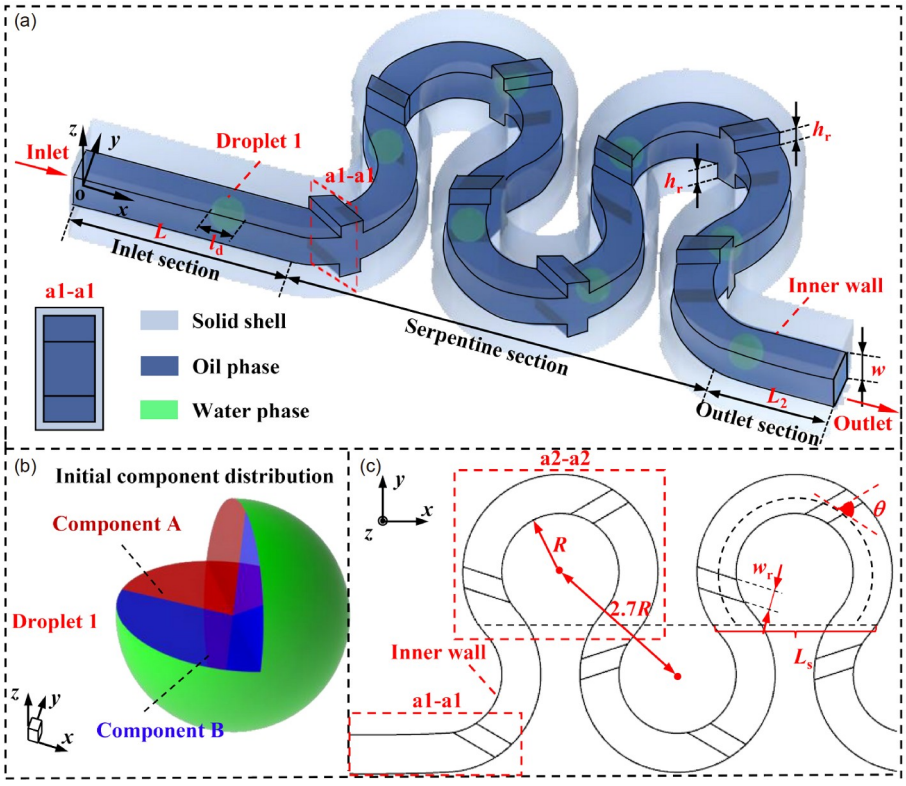

Figure 1 (Color online) Geometric schematic diagrams of SMR microchannel. (a) 3D drawing of SMR channel and its cross-section a1-a1 where L and L_2 are the length of inlet straight channel and outlet straight channel, respectively, h_r is the ridge height, w represents the microchannel width, l_d is the droplet length; (b) an enlarged cutaway view of the droplet 1 in (a); (c) top view of the fluid domain in the serpentine section where R is the radius of serpentine microchannel, w_r is the ridge width, and θ is the angle between the ridge and the tangent of curved channel.

2.2 Governing equations

Droplet mixing is a typical unsteady multiphase and multi-component flow problem, where the movement of liquid-liquid interfaces and 3D component mixing inside a droplet must be considered simultaneously [25,26]. To handle this problem, a coupled model of volume-of-fluid (VOF) method and component transport model was developed. The liquid-liquid (oil and water) interfaces were captured by the VOF method [27–29] and the flow motion was solved by the Navier-Stokes equation:

$$\frac{\partial \alpha_d}{\partial \tau} + \nabla \cdot (\alpha_d \mathbf{u}) = 0, \tag{1}$$

$$\frac{\partial \rho}{\partial \tau} + \nabla \cdot (\rho \mathbf{u}) = 0, \tag{2}$$

$$\frac{\partial (\rho \mathbf{u})}{\partial \tau} + \nabla \cdot (\rho \mathbf{u}\mathbf{u}) = -\nabla p + \rho \mathbf{g} + \nabla \cdot [\mu(\nabla \mathbf{u} + \nabla \mathbf{u}^{\mathrm{T}})] + \mathbf{F}, \tag{3}$$

where α_d is the volume fraction of the dispersed phase (i.e., the water phase), which consists of components A and B. The volume fraction of the oil phase is $\alpha_c = 1-\alpha_d$. $\mathbf{u}$, τ, p, $\mathbf{g}$, and $\mathbf{F}$ are the liquid velocity vector, flow time, liquid pressure, local acceleration vector of gravity, and source term of interfacial tension, respectively. Gravity effects are negligible owing to the much larger interfacial tension. The liquid density ρ and viscosity μ are defined as follows:

$$\rho = \rho_d \alpha_d + \rho_c \alpha_c, \tag{4}$$

$$\mu = \mu_d \alpha_d + \mu_c \alpha_c, \tag{5}$$

where the density ρ_c and dynamic viscosity μ_c of the oil phase are 960 kg/m^3 and 0.002 Pa s, respectively. As the physical properties of the two components in the water phase are identical, the density ρ_c and dynamic viscosity μ_c of the dispersed phase were set as constants with values of 998.2 kg/m^3 and 0.001 Pa s, respectively.

To model the interfacial tension at the oil-water interface, the continuous surface force (CSF) model presented by Brackbill et al. [30] was adopted, which converts the interfacial tension to the source term $\mathbf{F}$ of momentum equation, i.e., eq. (3), resulting in the following:

$$\mathbf{F} = \sigma \frac{2\rho\kappa}{\rho_d + \rho_c} \cdot \nabla \alpha_d, \tag{6}$$

where σ (0.01 N/m) and κ are the interfacial tension coefficient and the curvature of the oil-water interface, respectively.

$$\kappa = \nabla \cdot \hat{\mathbf{n}} = \nabla \cdot \left(\frac{\nabla \alpha_d}{|\nabla \alpha_d|} \right). \tag{7}$$

Because of the differences in the intermolecular forces

between silicone oil, water, and solids [31–33], there is a contact angle θ_w between the oil-water interface and the solid wall when they are in contact, which is considered by the contact angle model [30]. In the framework of the CSF model, the effects of the assumed contact angle are considered by adjusting the curvature of the fluid interface in the meshes near the microchannel walls using the following equation:

$$\hat{\mathbf{n}} = \mathbf{n}_w \cos\theta_w + \mathbf{T}_w \sin\theta_w, \tag{8}$$

where $\mathbf{n}_w$ and $\mathbf{T}_w$ are the normal and tangential vectors of the microchannel walls, respectively.

Based on the displacement of droplets in the SMR microchannel, the convective diffusion of components inside droplets is described by the component transport equation:

$$\frac{\partial(\alpha_d Y_A)}{\partial \tau} + \nabla \cdot (\alpha_d Y_A \mathbf{u}) = \nabla \cdot (\alpha_d D \nabla Y_A), \tag{9}$$

where Y_A denotes the mass fraction of component A inside the droplets, and the mass fraction of component B in the water phase is calculated by $Y_B = 1 - Y_A$. The diffusion coefficient D of component A in the water phase is given by 1.0×10^{-10} m^2/s [14].

2.3 Numerical solutions

The fluid domains shown in Figure 2 were extracted from the SMR microchannel depicted in Figure 1(a) by simplifying the solid shell as the inner wall. Non-slip boundary conditions were employed for the inner wall faces [34–36]. In the fluid domain, both oil and water phases were injected orderly from the left end face of the inlet section displayed in Figure 1(a), and the inlet velocity was set as follows:

$$u_{x,\text{in}} = u_m,\ u_{y,\text{in}} = 0,\ u_{z,\text{in}} = 0, \tag{10}$$

where u_m is a constant. The Reynolds number $Re = U_c D_h / \nu_c$ and capillary number $Ca = \rho_c \nu_c / \sigma$ were used to determine the flow state [37,38], where U_c and ν_c represented the flow velocity and kinematic viscosity of the oil phase, respectively. The hydraulic diameter D_h equals w for the square cross-section of SMR microchannels. To attain a series of equally sized droplets in SMR microchannels, a time-dependent function $\alpha_{d,\text{in}}(\tau)$ was applied to control the volume fraction of the water phase at the inlet:

$$\alpha_{d,\text{in}}(\tau) = \begin{cases} 0, & (m-\beta)T < \tau \leqslant mT, \\ 1, & (m-1)T \leqslant \tau < (m-\beta)T, \end{cases} \tag{11}$$

where m is the number of generated droplets, T is the generated period of a droplet, and β is the ratio of the inflow time of the oil phase to T. The right end face of the outlet section was set as a pressure outlet with atmospheric pressure, (i.e., 101325 Pa).

The entire fluid domain was discretized with hexahedral meshes and the detailed enlarged views are shown in Figure 2(b)–(d). To capture the thin oil-water interface and large velocity magnitude near the wall faces [39,40], the meshes were refined along the normal direction of the walls. To solve the governing equations under the above boundary conditions, the commercial computational fluid dynamics software ANSYS Fluent was adopted for its high-performance parallel computing. The VOF equation was discretized using

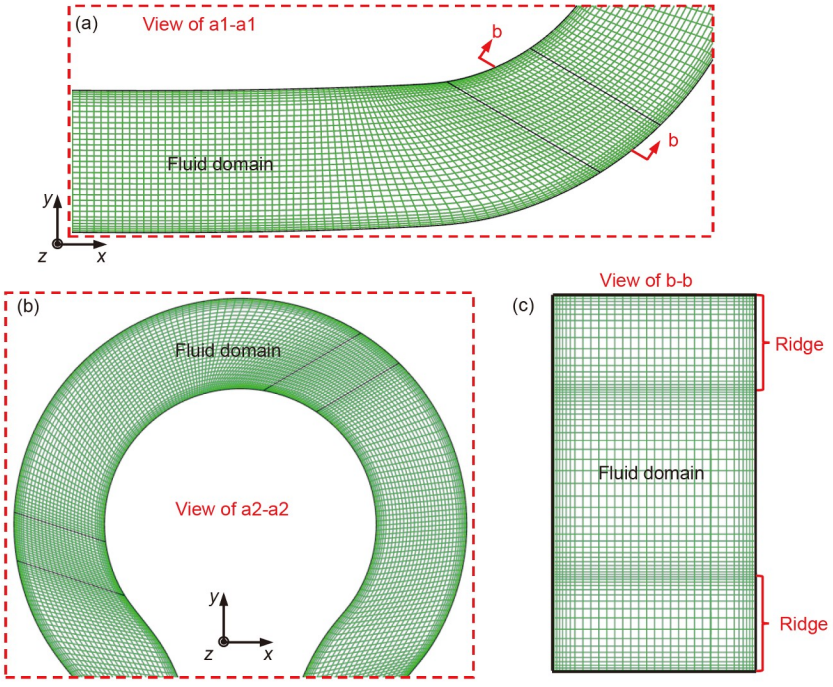

Figure 2 (Color online) Mesh illustration of SMR microchannel with 8 ridges on both top and bottom walls. (a) An enlarged view of the dotted box a1-a1 in Figure 1(c); (b) an enlarged view of the dotted box a2-a2 in Figure 1(c); (c) a cross-section view in (a).

an explicit scheme, and the oil-water interface was reconstructed using the geometric reconstruction scheme based on the piecewise linear method. The Pressure-Implicit with Splitting of Operators algorithm was utilized for pressure velocity coupling, and the second-order upwind scheme was employed for the spatial discretization of the momentum equation. The discretization of transient terms was achieved by a first-order implicit scheme. For unsteady numerical modeling, the important time step ($\Delta\tau$) was determined by the Courant number (<0.3) $CFL = (u\Delta\tau)/\Delta h$, where u is the flow velocity and Δh indicates the mesh size.

2.4 Model validation

To quantitatively validate the droplet mixing model, several dimensionless parameters were introduced to describe the droplet mixing characteristics. To evaluate the homogeneity of mixing, a mixing index M was defined as [13,41]

$$M = \left(1 - \frac{\delta}{\delta_0}\right) \times 100\%, \tag{12}$$

where δ is the mass fraction deviation of component A, which is equal to [16,42]

$$\delta = \sqrt{\sum_{i=1}^{n}\left[\left(Y_{A,i} - \overline{Y}_A\right)^2 V_i\right] / \sum_{i=1}^{n} V_i}, \tag{13}$$

where V_i and $Y_{A,i}$ are the volume and mass fraction of the mesh cell i inside a droplet, respectively. $\overline{Y}_A$ denotes the average mass fraction of component A within the droplet. The initial mass fraction deviation δ_0 (1 in this study) was calculated by the component distribution at the initial moment when mixing was not taken place. As the mixing tended to be homogenous, the relative mass fraction deviation δ/δ_0 decreased from 1 to 0, representing the homogenous mixing state. Thus, the range of mixing index M was 0–1 where the larger M means a more homogenous mixing. Moreover, the dimensionless displacement s^* of a droplet was set as the ratio of the droplet displacement s to the microchannel width w, where s was calculated from the inlet of the microchannels (see Figure 1(a)) to the center of mass of the droplet.

A mesh independence test was first performed to ensure that the numerical results were independent of the mesh density. As the mesh schemes used for all SMR microchannels were the same, an SMR microchannel with 8 ridges on the top and bottom walls was selected as a representative case for the mesh independence test. As depicted in Figure 3, the degree of deviation between two adjacent mixing curves decreased with increasing the mesh density, and the deviation between mesh numbers N = 1021500 and 1912300 was less than 3%, indicating that the effect of mesh density was therefore negligible. Concerning the computational cost, the mesh number N = 1021500 was employed for the discretization of the fluid domain.

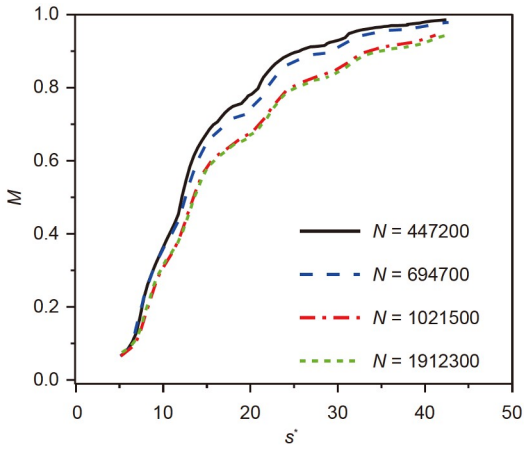

Figure 3 (Color online) Mixing curves for the droplet mixing (l_d^* = 1.5) in SMR microchannel with 8 ridges (w_r^* = 0.5) on both top and bottom walls (N = 447200, 694700, 1021500, and 1912300, at Re = 6.4, and Ca = 0.016) where M is the dimensionless index for evaluating the mixing homogeneity of the components inside droplets and ranges from 0 to 1 (a larger value means a more homogeneous mixing).

Furthermore, the numerical case using the above coupled model was compared with the experimental results presented by Jiang et al. [41]. In their experiment, a serpentine microchannel with a 50 μm × 40 μm cross-section (see Figure 4(a)) was filled with mineral oil with a density of 840 kg/m^3 and viscosity of 0.03 Pa s. An initial droplet consisting of two aqueous solutions (phosphate buffered saline labeled with two dyes, Alexa Fluor 430 and Lucifer yellow CH lithium salt [41]), was first generated by a two-phase flow-focusing structure, and then flowed through the serpentine section at a mean flow velocity of 41.7 mm/s. The density and viscosity of both aqueous solutions were the same with values of 1008 kg/m^3 and 0.00102 Pa s, respectively. The mixing processes inside a droplet flowing through the serpentine section were captured by a home-built two-photon fluorescence lifetime microscopy system [41]. Due to there being two dyes in the fluid, the mass fraction Y_{Alexa} was defined to represent the mass fraction of the fluids dyed by Alexa Fluor 430 at a point [41]. To model the mixing processes, a 3D computational domain with the same size and shape was constructed and discretized with structural hexahedral meshes. An initial 3D columned droplet with the same cross-section as that at position 1 was set. The initial droplet height was 30 μm and adjusted so that the fully developed droplet in modeling matched the size and shape of the droplet at position 1 in the experiment as depicted in Figure 4(b). A comparison of the evolution of component distributions of the experiments (see Figure 4(b)) and modeling (see Figure 4(c)) revealed that they were in good agreement with each other, demonstrating the same mixing pattern. There were differences between the experiment and simulation, as illustrated in Figure 4. The differences were caused by simplifications

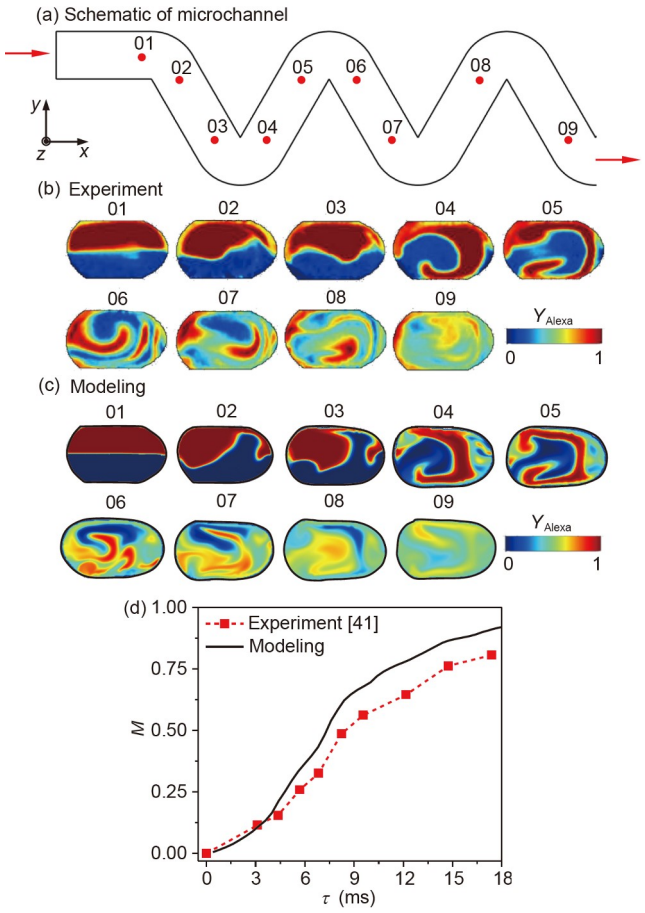

Figure 4 (Color online) Validation of the as-presented model by the experimental data in ref. [41] at the inlet velocity of 41.7 mm/s, where Y_{Alexa} is the mass fraction of the fluid dyed by Alexa Fluor 430, i.e., the mixing fraction defined in ref. [41]. (a) Schematic of the experimental microchannel [41]; (b) the contour of mass fraction inside the droplet captured in the experiment [41]; (c) the contour of mass fraction inside the droplet attained from the present simulation; (d) comparison of the mixing curves between the experiment and the simulation.

of the simulation conditions, such as a lack of consideration of the fluctuations in inlet velocity produced by the syringe pumps, manufacturing errors of the microchannel, and initial 3D component distributions inside droplets in the experiments. Although there were differences, their trends were the same and their component distributions and mixing curves (difference below 20%) were in reasonable agreement with each other, which supports the accuracy and reliability of the proposed numerical model.

3 Results and discussion

3.1 Enhancement mechanisms of droplet mixing in SMR microchannels

The current numerical studies indicate that compared with mixing inside droplets flowing through a smooth serpentine microchannel, droplet mixing in an SMR microchannel can be enhanced with the help of ridge structures that induce a unique flow field inside the droplets. Compared with the real flow field, a relative flow field attained by subtracting the overall droplet velocity from the real flow velocity is more intuitive for revealing the movement between two components [43]. According to the relative flow field and component contours, the mixing-enhancement process can be divided into three steps. First, component A in the middle of the droplet is entrained into the centrifugal side of the droplet by a pair of vortices. The vortices are induced by constriction of the droplet, as depicted in Figure 5(b) (the slice with a $0.9w_r$ distance from the ridge wall), when the droplet flows through the ridges. Second, under the effect of reverse flow in the ridges (as shown in Figure 5(c), namely, the slice with a $0.9h_r$ distance from the ridge wall), more of component A flows to the centrifugal side at the tail of the droplet that occurring in a smooth serpentine microchannel (see Figure 6(b) and (e)). Lastly, component A at the centrifugal side flows into the middle of component B due to non-horizontal vortices in the serpentine sections as shown in Figure 6(c) and (f), which is an important convection-diffusion process to enhance the mixing. In the convection-diffusion process, mixing is generally improved as the quantity of component A is increased at the centrifugal side of the droplet, which ensures efficient mixing performance of the SMR microchannel.

It can thus be concluded that efficient mixing in SMR microchannels is produced by two main factors: (1) the combined effects of the vortex pair and reverse flow in the ridge sections, providing reasonable wrapping between the inside component A and outside component B; and (2) component A wrapped by the outside component B flows into the middle of component B due to non-horizontal vortices in the serpentine sections.

3.2 Effects of ridge width on droplet mixing

As mentioned in Section 3.1, adding ridges on the wall of the smooth serpentine microchannel can improve droplet mixing, however, the effect of the geometric parameters of ridges, such as the ridge number and ridge width, on the mixing characteristics remains unclear. Therefore, the effect of ridge width on droplet mixing in an SMR microchannel with 8 ridges was studied. The width ratio w_r^* of ridges (0–1) was used to examine the mixing inside droplets with different length ratios l_d^*, including 1.0, 1.5, and 2.2.

Figure 7 displays the variations of mixing index M with the dimensionless displacement s^* of droplets in SMR microchannels at different w. As seen in Figure 7, there existed two different variations with increasing the width ratio w_r^* for different droplet lengths, namely, enhanced mixing for large droplets ($l_d^* > 1.0$) and weakened/enhanced mixing for small

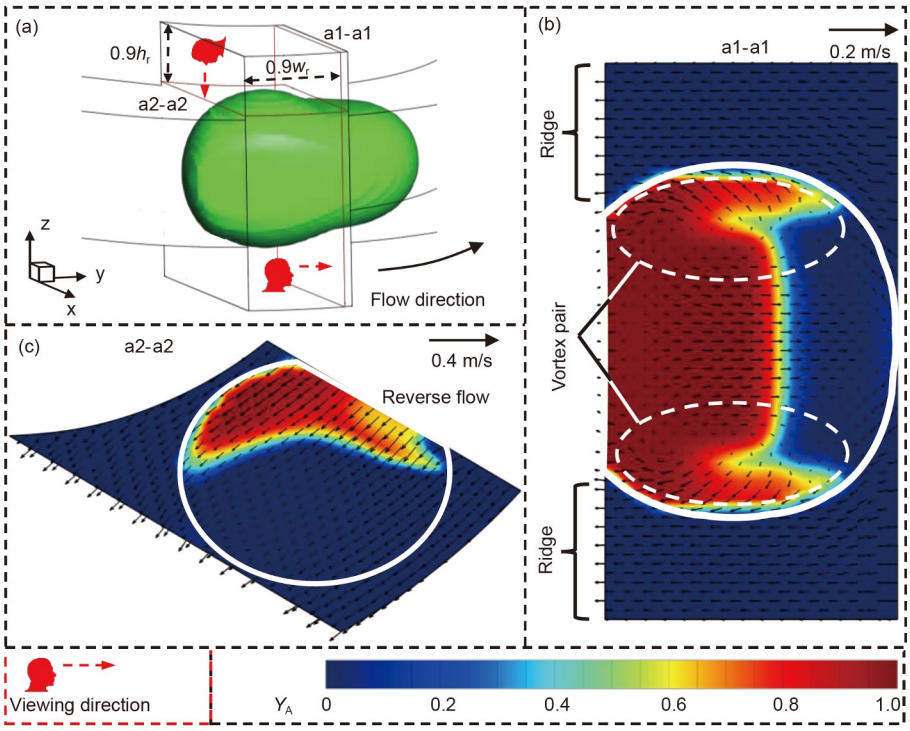

Figure 5 (Color online) Mixing inside droplet ($l_r^* = 2.2$) flowing through the first ridge ($s^* = 7.0$) of SMR microchannel with 8 ridges ($w_r^* = 0.75$) at $Re = 6.4$, and $Ca = 0.016$, where Y_A represents the mass fraction of component A in the fluids. (a) 3D morphology of a droplet and the spatial positions of the cross-sections; (b) relative velocity vector distribution and concentration contour at slice a1-a1 in (a); (c) relative velocity vector distribution and concentration contour at slice a2-a2 in (a).

droplets ($l_d^* = 1.0$). For droplets with $l_d^* > 1.0$, there is 6%–11.7% improvement in the mixing index M_{out} at the outlet of SMR microchannels compared with that for smooth serpentine microchannels (see Figure 7(d)). The mixing performance of SMR microchannels was determined by two mixing-enhancement factors, namely, the combined effects of the vortex pair and reverse flow in the ridge section (Figure 5) and non-horizontal vortices in the serpentine section (Figure 6). Because the two mixing-enhancement factors were mainly influenced by the abrupt constriction of the ridge sections, increasing w_r^* did not have a significant impact on droplet mixing, as seen in Figure 7(b) and (c). Therefore, the variations of droplet mixing versus w were not significant in the SMR microchannel. However, for a droplet with $l_d^* = 1.0$, mixing in the SMR microchannel was weakened when w was less than 0.75. The weakened mixing was attributed to the decreased component A wrapping outside component B, which was caused by the vanishing vortex pair inside the droplet. The maximum height ratio of the droplet to the microchannel h_d/w was defined to evaluate the degree of droplet deformation when the droplet flowed through the ridge sections. An h_d/w ratio greater than 1 signifies that the droplet is deformed, whereas an h_d/w ratio less than 1 signifies that the droplet is not deformed. As illustrated in Figure 8(a), the droplet with $l_d^* = 1.0$ droplet was not deformed, resulting in the disappearance of the vortex pair. However, when $w_r^* \geqslant 0.75$ at the middle slice ($z = w/2$) of the droplets as shown in Figure 9(a) and (c), droplet mixing was enhanced by the special outward movement of the inside component A along the radial direction. This movement was generated by the deceleration of droplets due to the broadened microchannel in the ridge structures. The decelerating processes are illustrated in the curved graph of the dimensionless velocity magnitude of the droplets, i.e., Figure 8(b), where u_m is the average velocity of droplets in the microchannel. As depicted in Figure 8(b), significant velocity fluctuations only arose in the ridge sections when $w_r^* \geqslant 0.75$. In summary, when the droplet length was greater than the microchannel, the droplet mixing performance of SMR microchannels was better than that of smooth serpentine microchannels and the effect of the ridge width ratio on mixing was insignificant. For droplets with a length equals to the microchannel width, the ridge structure had a negative effect on droplet mixing when the ridge width ratio was $w_r^* < 0.75$, however, it had a positive effect when the ridge width ratio was $w_r^* \geqslant 0.75$.

To comprehensively evaluate the performance of microchannels, the mixing characteristics and hydrodynamic characteristics must be considered simultaneously. The pressure loss of the entire microchannel is an important hydrodynamic parameter, in the design of microfluidics systems [44]. Here, to characterize the pressure loss for the

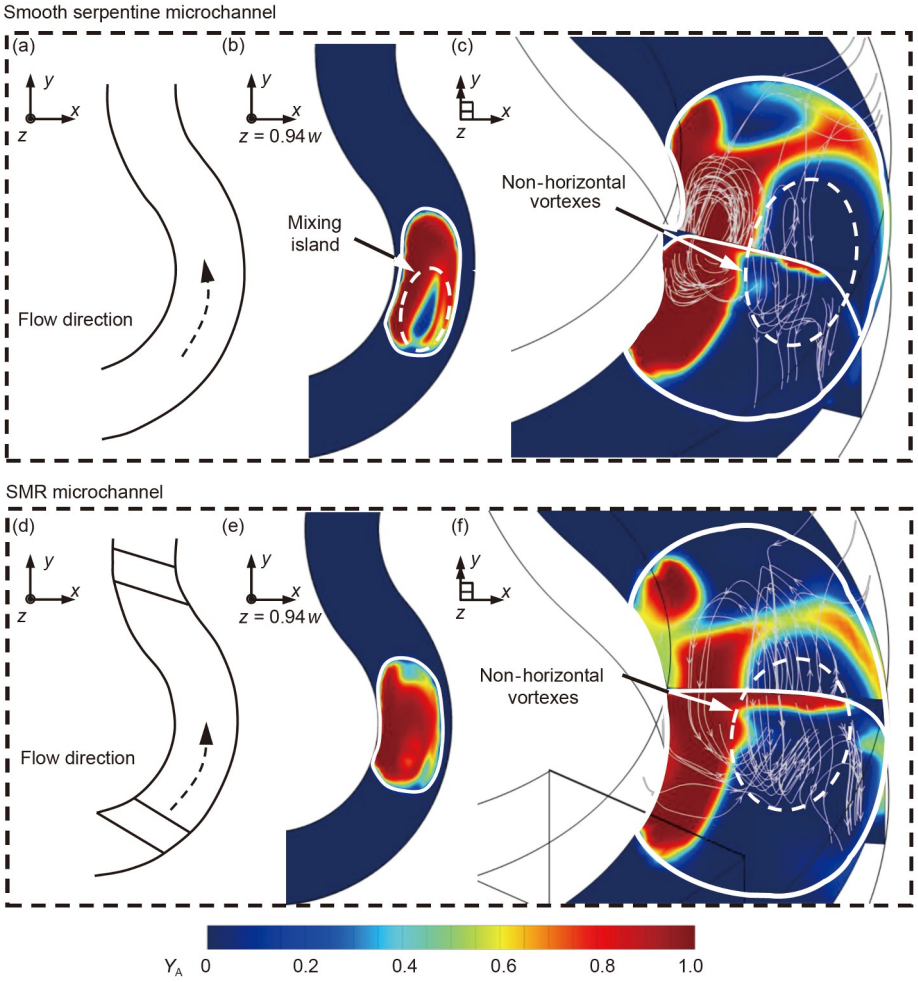

Figure 6 (Color online) Comparisons of the concentration contours and 3D streamlines inside the droplet ($l_d^* = 2.2$) flowing through SMR microchannel with 8 ridges ($w_r^* = 0.75$) and the smooth serpentine microchannel ($s^* = 8.5$, at $Re = 6.4$, and $Ca = 0.016$), where Y_A is the mass fraction of component A in the fluid and ranges from 0 to 1. (a)–(c) The smooth serpentine channel; (d)–(f) SMR channel.

liquid-liquid flow developed by the straight inlet section, a dimensionless apparent friction factor f was introduced:

$$f = \frac{2D_h \Delta \overline{p}}{\rho_m L_s u_m^2}, \tag{14}$$

where ρ_m and u_m represent the average density and average longitudinal velocity of the fluid, respectively. L_s denotes the length of the SMR serpentine microchannel and smooth serpentine microchannel. It should be noted that the pressure drop between the inlet and outlet fluctuated periodically due to the hydrodynamic unevenness of periodic two-phase flow. To avoid the influence of periodic fluctuation, the mean pressure drop $\Delta \overline{p} = \int_T \Delta p \mathrm{d}\tau / T$ was calculated during a long period ($10T$, i.e., 10 generation periods of droplets), where Δp is the transient pressure drop between the inlet and outlet in a period T. Combining the apparent friction factor f and mixing index M, a comprehensive index, i.e., the dimensionless mixing efficiency E was defined as follows:

$$E = \frac{M_{out,s}/f_s}{M_{out,cs}/f_{cs}}, \tag{15}$$

where subscripts s and cs represent the SMR microchannel and smooth serpentine microchannel, respectively.

As seen in Figure 10(a), the apparent friction factor f showed a downward trend with an increase in w_r^* for a droplet with $l_d^* = 1.0$, which may be caused by the drag-reducing effect of the ridge structure (i.e., a rectangular groove) [45]. Thus, less pump power is used to maintain the same flow rate for droplet flow ($l_d^* = 1.0$) in SMR microchannels with wider ridges. The minimum of f (at $w_r^* = 1.0$) was lower than that in a smooth serpentine microchannel by approximately 8%. However, for droplets with large l_d^* (> 1.0), f first increased due to the deformation of droplets in the ridge sections and then decreased as a result of the augmentation of ridge width. Compared with the smooth serpentine microchannel, the maximum increment of f was only 6% (at $l_d^* = 1.5$ and $w_r^* = 0.25$) for large droplets. The

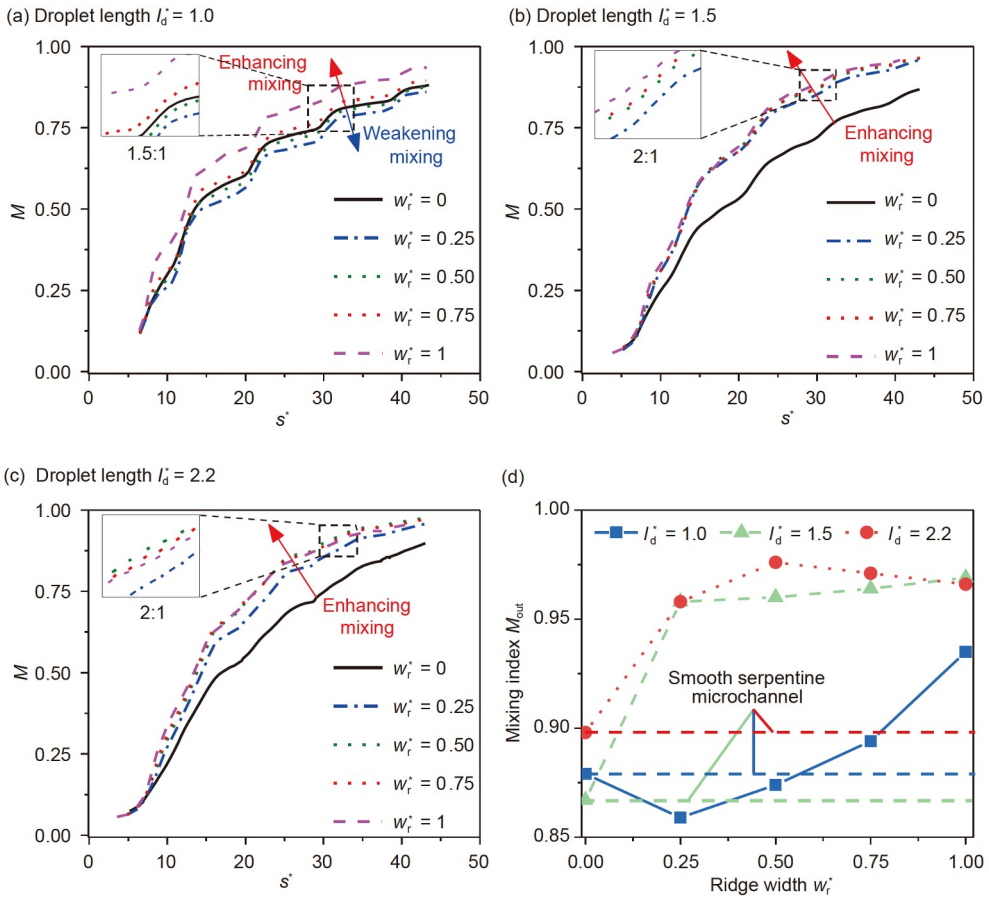

Figure 7 (Color online) Effects of the width ratio w_r^* of the ridges on the mixing index M for the droplets with different l_d^* (at Re = 6.4, and Ca = 0.016). (a) l_d^* = 1.0 and the 1.5× magnified insert of mixing curves; (b) l_d^* = 1.5 and the 2.0× magnified insert of mixing curves; (c) l_d^* = 2.2 and the 2.0× magnified insert of mixing curves; (d) variations of the mixing index at the outlet M_{out} (s^* = 43) versus w_r^*.

increment of pressure loss at a range of w = 0–1 was small (⩽ 6%). For droplets with different l_d^*, the mixing efficiency E showed an increasing trend with increasing the ridge width ratio. The mixing efficiency was improved by 3.6%–16% compared with that in the smooth serpentine microchannel, as depicted in Figure 10(b). In particular, there was a maximum 16% increase in mixing efficiency at l_d^* = 1.0 and w_r^* = 1.0, which was caused by the special component movement as seen in Figure 9(c).

3.3 Effect of ridge number on droplet mixing

Increasing the ridge number causes to augment the overall ridge width, however, its effect on the droplet mixing is different from that of increasing the ridge width due to complex interactions between the droplet and ridges. The detailed mixing and hydrodynamic characteristics of SMR microchannels with various ridge numbers must be studied to further enhance the mixing. Here, a ridge with a ratio w_r^* = 0.25 (i.e., the case with the lowest mixing efficiency) was selected to study the effect of the ridge number on droplet mixing.

As illustrated in Figure 11, there were two opposite trends of droplet mixing with increasing the ridge number for different droplet lengths l_d^*. Specifically, mixing was weakened when l_d^* = 1.0, but it enhanced when l_d^* > 1.0. The negative effects of the ridge structure on mixing inside the droplet with l_d^* = 1.0 were accumulated when the ridge number was increased. Component A entraining into component B at the centrifugal side of droplets S1–S3, as shown in Figure 12 (the full mixing processes are illustrated in Movies S1), decreased with an increased ridge number due to the accumulation of negative effects. However, for droplets with l_d^* > 1.0, because of the positive effect of a single ridge on droplet mixing, the "mixing island" of droplet L1, as shown in Figure 12(c), was broken with increasing the ridge number which resulted in better mixing (see droplet L2 in Figure 12(f) and droplet L3 in Figure 12(i)). With an increase in the ridge number, the apparent friction factor f decreased for small droplets (l_d^* = 1.0), and first increased and then declined for large droplets (l_d^* > 1.0), which was similar to the variation caused by increasing the ridge width. The maximum increment of f was less than 6% compared with that for a smooth

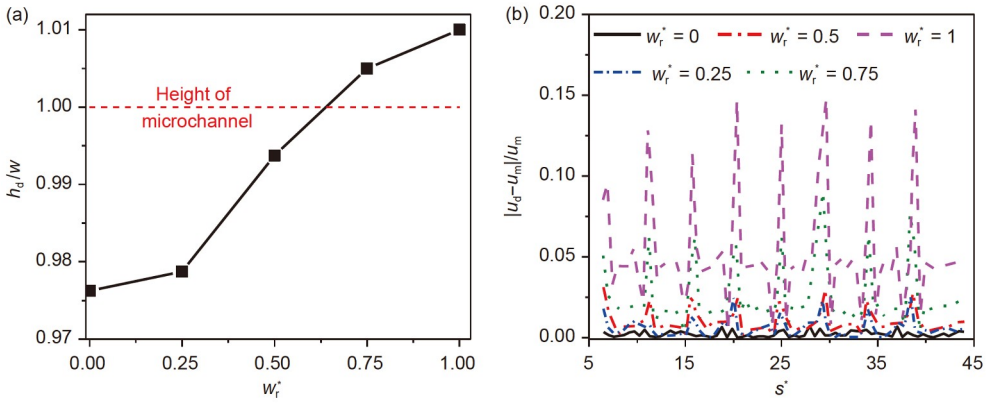

Figure 8 (Color online) Hydrodynamic and geometric characteristics of a droplet (l_d^* = 1.0) flowing through SMR channels with different ridge widths. (a) Variation of the maximum height ratio of the droplet to microchannel with w_r^*; (b) variation of the relative velocity of the entire droplet with the dimensionless displacement s^*.

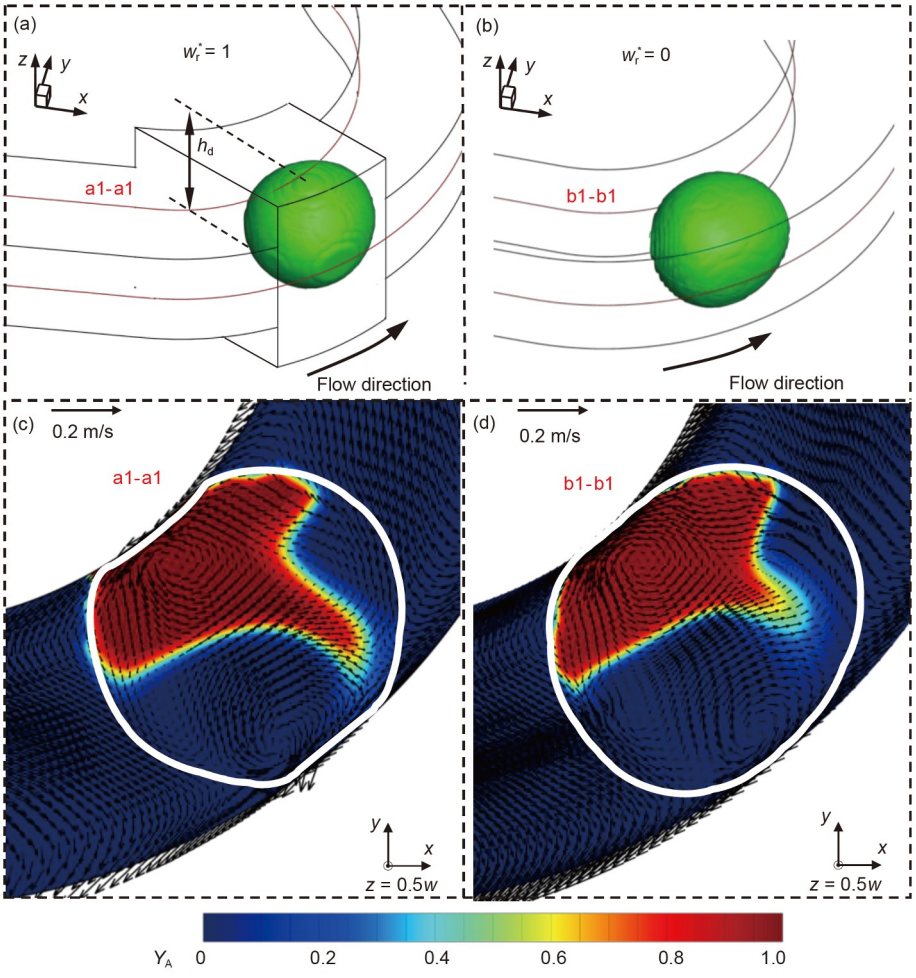

Figure 9 (Color online) Comparisons of the concentration contours and relative velocity vector fields inside a droplet (l_d^* = 1.0) flowing through SMR microchannel with 8 ridges (w_r^* = 1.0) and the common serpentine microchannel (s^* = 7.03, at Re = 6.4, and Ca = 0.016). (a) 3D droplet in the SMR channel; (b) 3D droplet in the smooth serpentine channel; (c) the concentration contours and relative velocity vector fields in the slice of $z = 0.5w$ for the SMR channel; (d) the concentration contours and relative velocity vector fields in the slice of $z = 0.5w$ for SMR channel.

serpentine microchannel, as depicted in Figure 13(a),and thus, the increase in pressure loss was insignificant. So, the augmentation of mixing efficiency E is determined by enhanced droplet mixing in SMR microchannels. As seen in Figure 13

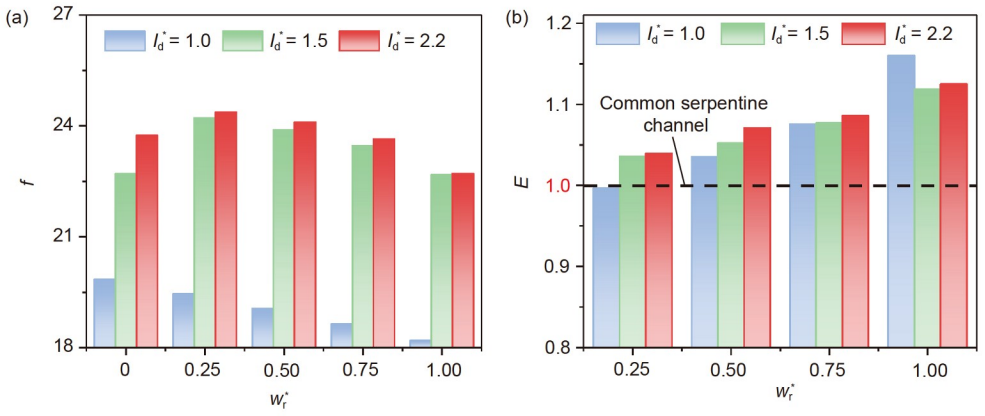

Figure 10 (Color online) Variation of (a) the apparent friction factor f, (b) mixing efficiency E versus the ridge width w_r^* for various droplet length ratios (Re = 6.4, Ca = 0.016).

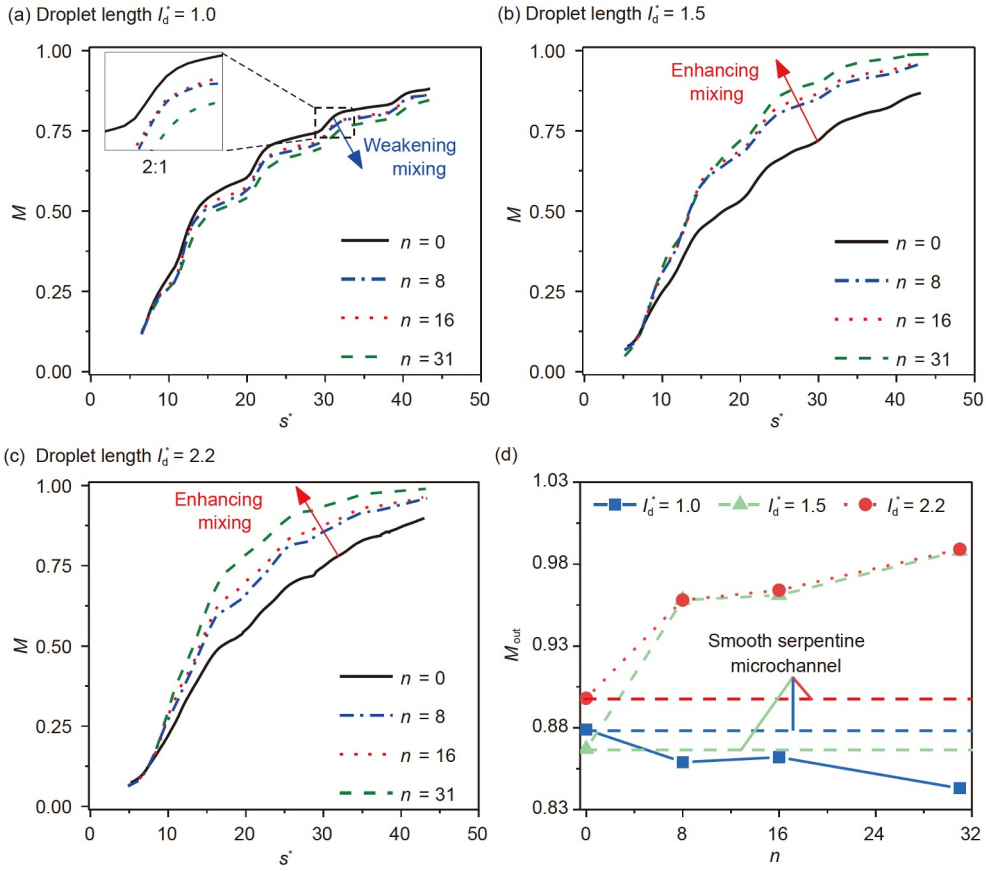

Figure 11 (Color online) Effects of the ridge number n on the mixing index M for the droplets with different droplet lengths l_d^* (at Re = 6.4, and Ca = 0.016). (a) l_d^* = 1.0 and the 2.0× magnified insert of mixing curves; (b) l_d^* = 1.5; (c) l_d^* = 2.2; (d) variations of the mixing index at the outlet M_{out} (s^* = 43) versus n.

(b), the variation of mixing efficiency E against ridge number was similar to that of mixing index M_{out}. For large droplets (l_d^* > 1.0), the mixing efficiency was enhanced by increasing the ridge number. But, for small droplets (l_d^* = 1.0), the mixing efficiency was not significantly improved and even weakened.

In summary, the positive or negative effects of a ridge on mixing inside droplets are accumulated as the augmentation of ridge numbers. For a small droplet (l_d^* = 1.0), with increasing the ridge number, the poor mixing performance in SMR microchannels is worsened, whereas, for a large droplet (l_d^* > 1.0), the good mixing performance in SMR microchannels is enhanced. With increasing the ridge number, changes in pressure loss in the SMR microchannel are not

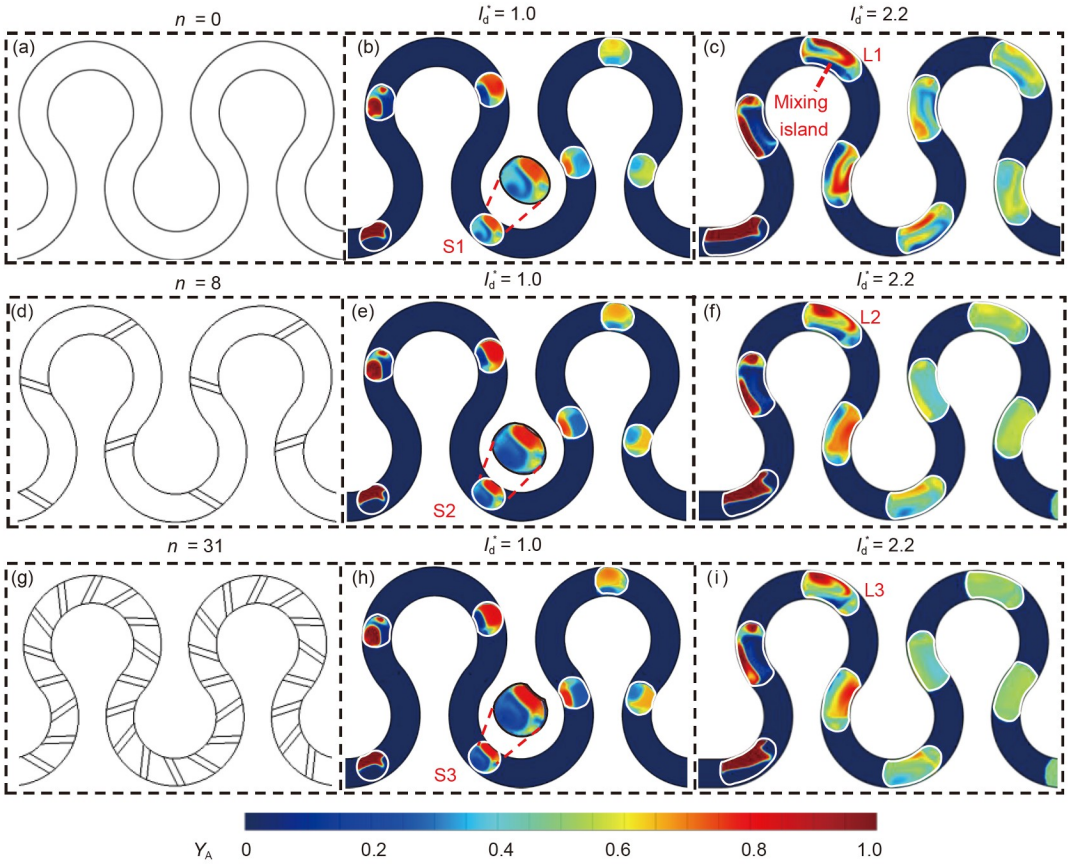

Figure 12 (Color online) Concentration contours in the middle slice ($z = h/2$) and top views of SMR microchannels with different ridge numbers (Re = 6.4, Ca = 0.016). (a)–(c) n = 0; (d)–(f) n = 8; (g)–(i) n = 31.

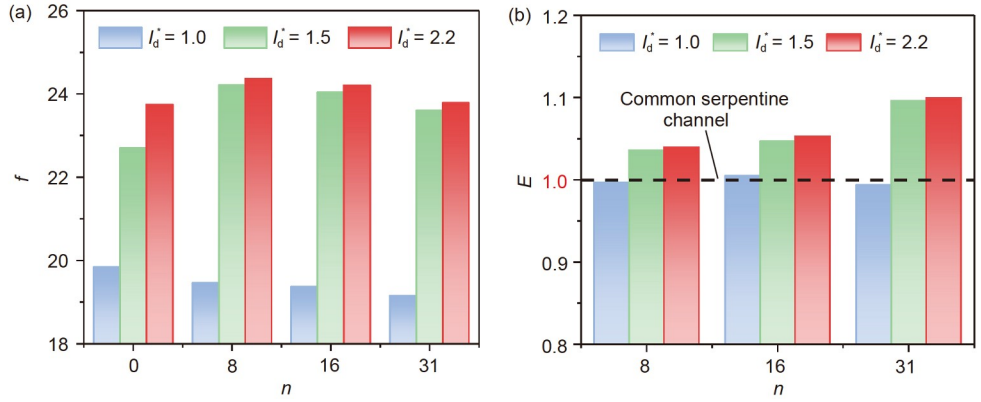

Figure 13 (Color online) Variation of (a) the apparent friction factor f, (b) mixing efficiency E versus the ridge number for various droplet length ratios (Re = 6.4, Ca = 0.016).

significant. The mixing efficiency of the SMR microchannel is determined by the mixing characteristics. To improve the mixing efficiency, the ridge number must be reduced for small droplets and increased for large droplets.

4 Conclusions

This work numerically investigated 3D droplet mixing in serpentine microchannels with ridges on the top and bottom walls (referred to as SMR microchannels) using a coupled model of the VOF method and component transport model. Based on the numerical simulation, the underlying mechanisms of droplet mixing in SMR microchannels were revealed. Moreover, the effects of two important geometric parameters of ridges (i.e., ridge width and ridge number) on the flow and mixing characteristics inside droplets with different sizes were clarified. In addition, the highly efficient

mixing performance of SMR microchannels under different conditions was observed. The main conclusions are as follows.

(1) Droplet mixing in SMR microchannels is mainly determined by two factors: the combined effects of the vortex pair and reverse flow inside the droplets during flow through the ridge sections, and the effects of non-horizontal vortices inside the droplets during flow through the serpentine sections.

(2) Both the droplet length and ridge width are vital for determining the droplet mixing performance of the SMR microchannel. When the droplet length is greater than the microchannel width, the mixing performance of the SMR microchannel with different ridge widths is enhanced owing to the above two mixing-enhancement factors. So, the ridges have a positive effect on the mixing, and there is 6.0%–11.7% and 3.6%–12.5% improvement in mixing indices at the outlet and mixing efficiency, respectively, compared with that in a smooth serpentine microchannel. However, when the droplet length is equal to the microchannel width, the combined effects of the vortex pair and reverse flow in the ridge sections tend to vanish. Therefore, mixing becomes worse than that in a smooth serpentine microchannel, and the ridges have a negative effect on mixing until a significant velocity fluctuation of the droplets is caused by increasing the ridge width. The significant velocity fluctuation caused when the ridge width equals the microchannel width leads to a maximum 16.0% increase in mixing efficiency.

(3) Because of the positive/negative effects of a single ridge in the SMR microchannel (i.e., enhanced/weakened mixing inside droplets with a length larger/smaller than the microchannel width), there are two opposite mixing performances with increasing the ridge number. For a small droplet with a length equal to the microchannel width, the droplet mixing performance decreases with increasing the ridge number, which is the result of the accumulation of the negative effect of the ridges on mixing in small droplets. But, when the droplet length is greater than the microchannel width, the droplet mixing performance is enhanced due to the accumulation of the above positive effect of the ridges, and there is 3.5%–10% improvement in mixing efficiency.

In this paper, the mixing-enhancement mechanisms of SMR microchannels are revealed, which is helpful for understanding the complex chaotic droplet mixing behavior in microchannels. In particular, according to the mixing characteristics, the addition of ridges in a serpentine microchannel can produce mixing-enhancement effects without a large increase in pressure loss. Therefore, the addition of a ridge structure is useful for developing more efficient microfluidic mixing devices. Moreover, the mixing characteristics of different droplet sizes in SMR microchannels with various ridge numbers and widths are clarified, which is meaningful to designing more efficient droplet-mixing microchannels by the addition of ridge structure.

This work was supported by the National Natural Science Foundation of China (Grant Nos. 51725602 and 52036006).

Supporting Information

The supporting information is available online at tech.scichina.com and link.springer.com. The supporting materials are published as submitted, without typesetting or editing. The responsibility for scientific accuracy and content remains entirely with the authors.

1 Churski K, Korczyk P, Garstecki P. High-throughput automated droplet microfluidic system for screening of reaction conditions. Lab Chip, 2010, 10: 816–818
2 Casadevall i Solvas X, deMello A. Droplet microfluidics: Recent developments and future applications. Chem Commun, 2011, 47: 1936–1942
3 Song H, Ismagilov R F. Millisecond kinetics on a microfluidic chip using nanoliters of reagents. J Am Chem Soc, 2003, 125: 14613–14619
4 Song H, Chen D L, Ismagilov R F. Reactions in droplets in microfluidic channels. Angew Chem Int Ed, 2006, 45: 7336–7356
5 Sarrazin F, Prat L, Di Miceli N, et al. Mixing characterization inside microdroplets engineered on a microcoalescer. Chem Eng Sci, 2007, 62: 1042–1048
6 Liau A, Karnik R, Majumdar A, et al. Mixing crowded biological solutions in milliseconds. Anal Chem, 2005, 77: 7618–7625
7 Grigoriev R O, Schatz M F, Sharma V. Chaotic mixing in microdroplets. Lab Chip, 2006, 6: 1369–1372
8 Gissinger J R, Zinchenko A Z, Davis R H. Internal circulation and mixing within tight-squeezing deformable droplets. Phys Rev E, 2021, 103: 043106
9 Song H, Tice J D, Ismagilov R F. A microfluidic system for controlling reaction networks in time. Angew Chem Int Ed, 2003, 42: 768–772
10 Aref H, Blake J R, Budišić M, et al. Frontiers of chaotic advection. Rev Mod Phys, 2017, 89: 025007
11 Stone Z B, Stone H A. Imaging and quantifying mixing in a model droplet micromixer. Phys Fluids, 2005, 17: 063103
12 Bringer M R, Gerdts C J, Song H, et al. Microfluidic systems for chemical kinetics that rely on chaotic mixing in droplets. Philos Trans R Soc London Ser A-Math Phys Eng Sci, 2004, 362: 1087–1104
13 Bai L, Fu Y, Yao M, et al. Enhancement of mixing inside ionic liquid droplets through various micro-channels design. Chem Eng J, 2018, 332: 537–547
14 Ghazimirsaeed E, Madadelahi M, Dizani M, et al. Secondary flows, mixing, and chemical reaction analysis of droplet-based flow inside serpentine microchannels with different cross sections. Langmuir, 2021, 37: 5118–5130
15 Yin B, Luo H. Numerical simulation of drops inside an asymmetric microchannel with protrusions. Comput Fluids, 2013, 82: 14–28
16 Tanthapanichakoon W, Aoki N, Matsuyama K, et al. Design of mixing in microfluidic liquid slugs based on a new dimensionless number for precise reaction and mixing operations. Chem Eng Sci, 2006, 61: 4220–4232
17 Ottino J M, Muzzio F J, Tjahjadi M, et al. Chaos, symmetry, and self-similarity: Exploiting order and disorder in mixing processes. Science, 1992, 257: 754–760
18 Song H, Bringer M R, Tice J D, et al. Experimental test of scaling of mixing by chaotic advection in droplets moving through microfluidic channels. Appl Phys Lett, 2003, 83: 4664–4666
19 Wang J, Wang J, Feng L, et al. Fluid mixing in droplet-based microfluidics with a serpentine microchannel. RSC Adv, 2015, 5:

104138–104144
20 Cao X, Zhou B, Yu C, et al. Droplet-based mixing characteristics in bumpy serpentine microchannel. Chem Eng Processing-Process Intensification, 2021, 159: 108246
21 Olbricht W L, Leal L G. The creeping motion of immiscible drops through a converging/diverging tube. J Fluid Mech, 1983, 134: 329–355
22 Gai Y, Khor J W, Tang S K Y. Confinement and viscosity ratio effect on droplet break-up in a concentrated emulsion flowing through a narrow constriction. Lab Chip, 2016, 16: 3058–3064
23 Stroock A D, Dertinger S K W, Ajdari A, et al. Chaotic mixer for microchannels. Science, 2002, 295: 647–651
24 Chen Y, Yao F, Huang X. Mass transfer and reaction in methanol steam reforming reactor with fractal tree-like microchannel network. Int J Heat Mass Transfer, 2015, 87: 279–283
25 Shimokusu T J, Maybruck V G, Ault J T, et al. Colloid separation by CO_2-induced diffusiophoresis. Langmuir, 2020, 36: 7032–7038
26 Liu Z H, Xu H Z, Chen W C, et al. Dispersion characteristics of liquid jet impacting on the rotating single-layer wire mesh with different surface wettabilities. Chem Eng Sci, 2022, 251: 117495
27 Hirt C W, Nichols B D. Volume of fluid (vof) method for the dynamics of free boundaries. J Comput Phys, 1981, 39: 201–225
28 Wang J X, Yu W, Wu Z, et al. Physics-based statistical learning perspectives on droplet formation characteristics in microfluidic cross-junctions. Appl Phys Lett, 2022, 120: 204101
29 Cao Y H, Xin M. Numerical simulation of ice accretion in supercooled large droplet conditions. Sci China Tech Sci, 2019, 62: 1191–1201
30 Brackbill J U, Kothe D B, Zemach C. A continuum method for modeling surface tension. J Comput Phys, 1992, 100: 335–354
31 Shang L, Yu Y, Gao W, et al. Bio-inspired anisotropic wettability surfaces from dynamic ferrofluid assembled templates. Adv Funct Mater, 2018, 28: 1705802
32 Wang J X, Birbarah P, Docimo D, et al. Nanostructured jumping-droplet thermal rectifier. Phys Rev E, 2021, 103: 023110
33 Chen Y, Zhang C, Shi M, et al. Slip boundary for fluid flow at rough solid surfaces. Appl Phys Lett, 2012, 100: 074102
34 Giacomin A J, Jbara L M, Saengow C. Pattern method for higher harmonics from macromolecular orientation in oscillatory shear flow. Phys Fluids, 2020, 32: 011703
35 Cao X, Hao G, Li Y, et al. On male urination and related environmental disease transmission in restrooms: From the perspectives of fluid dynamics. Sust Cities Soc, 2022, 80: 103753
36 Wang J X, Cao X, Chen Y P. An air distribution optimization of hospital wards for minimizing cross-infection. J Clean Prod, 2021, 279: 123431
37 Song Y, Liu Q, Wang Z, et al. Super-wetting enabled by an array of SU-8 micro-pillars etched with ion-beam. J Micromech Microeng, 2020, 30: 115010
38 Yin Q, Guo Q, Wang Z, et al. 3D-printed bioinspired cassie-baxter wettability for controllable microdroplet manipulation. ACS Appl Mater Interfaces, 2021, 13: 1979–1987
39 Tian F B, Dai H, Luo H, et al. Fluid-structure interaction involving large deformations: 3D simulations and applications to biological systems. J Comput Phys, 2014, 258: 451–469
40 Jiang C B, Deng B, Hu S X, et al. Numerical investigation of swash zone hydrodynamics. Sci China Tech Sci, 2013, 56: 3093–3103
41 Jiang L, Zeng Y, Zhou H, et al. Visualizing millisecond chaotic mixing dynamics in microdroplets: A direct comparison of experiment and simulation. Biomicrofluidics, 2012, 6: 012810
42 Xia H M, Wan S Y M, Shu C, et al. Chaotic micromixers using two-layer crossing channels to exhibit fast mixing at low Reynolds numbers. Lab Chip, 2005, 5: 748–755
43 Maleki M A, Soltani M, Kashaninejad N, et al. Effects of magnetic nanoparticles on mixing in droplet-based microfluidics. Phys Fluids, 2019, 31: 032001
44 Verma R K, Ghosh S. Effect of phase properties on liquid-liquid two-phase flow patterns and pressure drop in serpentine mini geometry. Chem Eng J, 2020, 397: 125443
45 Mohammadi A, Floryan J M. Pressure losses in grooved channels. J Fluid Mech, 2013, 725: 23–54